UO2 micron scale specimen fracture: Parameter identification and influence of porosities

Aurélien Doitrand, Ronan Henry, Isabelle Zacharie-Aubrun, Jean-Marie Gatt, Sylvain Meille

UO_2 micron scale specimen fracture: Parameter identification and influence of porosities.

Aurelien Doitrand[a,*], Ronan Henry[a,b], Isabelle Zacharie-Aubrun[b], Jean-Marie Gatt[b], Sylvain Meille[a]

[a] *Université Lyon, INSA-Lyon, MATEIS UMR CNRS 5510, F-69621 Villeurbanne Cedex, France*
[b] *CEA, DES, IRESNE, DEC, Cadarache, F-13108 St Paul Lez Durance, France*

Abstract

Bending of micron-scale cantilevers with or without initial notch is simulated by finite element and their fracture is assessed using either the coupled criterion or a cohesive zone model. The fracture toughness and strength of UO_2 single grain specimens with several crystal orientations are determined by means of inverse identification based on experimental tests at the micron-scale. Irradiation causes a decrease in fracture toughness from around 10 J/m^2 to around 5 J/m^2, whereas the strength variation remains in the order of magnitude of the measurement uncertainty. Premature fracture may occur in presence of a pore provided it is located close enough to the specimen surface undergoing tension, the resulting failure force decreasing with increasing pore size. A network of small porosities located on the fracture surface induces a decrease in the failure force which magnitude mainly depends on the total surface fraction and on the porosity locations rather than on the porosity size.

Keywords: Micron scale cantilevers; Irradiation; Nuclear fuel; Porosities ; Coupled criterion ; Cohesive zone model

1. Introduction

The nuclear fuel commonly used in Pressurized Water Reactors (PWR) is uranium dioxide UO_2 shaped in the form of pellets. This ceramic material is brittle at temperatures below 1000°C and systematically cracks during the first power rise of the reactor. Indeed, during service, the heat produced by the nuclear reaction is transferred to the coolant by thermal

conduction through the cladding. Then, for standard operating conditions, the temperature is around 1000°C at the pellet core and 500°C at its periphery, this strong thermal gradient inducing the pellet fracture. For unconventional operating phases, such as power ramps or accidental situations simulated in laboratory Material Test Reactor (MTR), the additional temperature rise leads to additional cracking, respectively at the pellet periphery [1], in the entire pellet [2] and at the grain boundaries [3].

In order to improve the numerical modelling of the fuel behavior in reactor, for instance for the simulation of the pellet-cladding interaction [4], it is of primary importance to characterize the fracture properties of the fuel and their variation due to irradiation. The main parameters of interest are the strength and the fracture toughness [5]. These two properties have already been identified on the fresh fuel (before irradiation in reactor) by conventional measurement methods on macroscopic specimens [6–8]. However, the irradiation induced cracking of the pellets makes it impossible to perform such measurements on irradiated specimens at the macroscopic scale.

The recent development of micromechanical tests on irradiated fuels has given access to their local fracture properties [9, 10], employing a micro-cantilever bending method initially developped by Di Maio *et al.* [11]. However, because of the micrometric dimensions of the specimens, scale effects are observed on the fracture stress compared to larger specimens. The stress locally attained in micron scale is generally much larger than the one at the macroscopic scale [12]. This phenomenon can be attributed, on the one hand, to fewer and smaller defects [13–15], and on the other hand to smaller available elastic energy for fracture [16, 17]. This type of experiments makes it possible to test unconventional configurations such as uncracked volumes of irradiated UO_2, but also requires the set-up of dedicated post-processing methods in order to obtain quantitative data to be used for the numerical approaches for failure prediction.

Numerical simulation of fracture can be employed to set up such inverse identification approaches. Several modeling methods exist such as, for instance, cohesive zone model (CZM) [18, 19] or approaches based on finite fracture mechanics such as the coupled criterion (CC) [16, 20]. Both approaches are particularly adapted to model fracture along a known crack path. Other approaches such as XFEM [21], thick level set [22] or phase-field approach for

fracture [23–25] can also be employed if the crack path is not known a priori. Several authors compared CC and CZM [26–32]. In particular Martin *et al.* [33] showed that both methods yield similar results provided the characteristic material length is small enough [34]. Doitrand *et al.* [28] highlighted the possibility to identify a CZM profile by confronting the initiation loading level and crack arrest length. Both methods were also jointly used by Ricardo *et al.* [35] for the simulation of thermal shock induced cracking in ceramics. The CC appears to be computationally very efficient compared to CZM, mainly in 2D cases [28] or in 3D if the crack surfaces can easily be determined [36–38]. In cases where the crack can be described by several parameters [39] or that the crack front cannot be easily obtained, CZM may however be more efficient especially if the crack path is known.

The objective of this work is twofold: on the one hand, it aims at identifying the fracture parameters of fresh and irradiated UO_2 based on micro-cantilever experimental tests. On the other hand, it aims at studying the influence of porosities on the specimen failure. In Section 2, we describe the micro-cantilever experiments. The approaches for fracture simulation as well as the finite element (FE) models are described in Section 3. Section 4 is dedicated to fresh and irradiated UO_2 fracture parameter identification. The influence of porosities on the specimen failure is presented in Section 5.

2. Experiments

2.1. Materials

Two series of specimens are analyzed, all the specimens of a series being prepared from the same sample. The first type of specimen is made of a fresh (non-irradiated) UO_2, referred to as $^{\mathrm{F}}UO_2$ in the sequel. The second type of specimens is UO_2 irradiated in PWR at a 34 GWd/tU average burn-up and is referred as to $^{\mathrm{I}}UO_2$. This last fuel has a Cr_2O_3 doping, which allows a considerable increase in grain size during sintering but has almost no influence on the mechanical properties measured inside the grains [10]. Indeed, Cr_2O_3 doping represents very small quantities (less than 0.1%wt). This doping mainly improves the fuel creep resistance [40], which results from grain size change during sintering. Therefore, it is likely that doping has almost no influence on the mechanical properties of single grain micron-scale specimens.

2.2. Specimen preparation

Micro-cantilevers (Fig. 1) are prepared with a Focalised Ion Beam (FIB) of a shielded dual beam microscope Auriga 40 (Carl Zeiss, Oberkochen, Germany) in the hot cells of the CEA LECA-STAR facility at Cadarache (France). Every specimen is prepared into fresh or irradiated UO_2 single grain with a chosen crystal orientation in order to control the fracture crystal plane. Two kinds of specimens are prepared, either with or without initial notch (Fig. 1). The manufacturing process is optimized so that the surface of the specimen sees as few ions as possible. Specimens without initial notch may therefore be slightly influence by ion implantation, which cannot be avoided at the notch of specimens containing an initial notch. Experimental studies demonstrated that ion implantation has almost no influence on the measured UO2 fracture toughness [9, 10], which may not always be the case for other materials [41–43]. A detailed description of the manufacturing process can be found in [9] and [10]. The specimen dimensions are summarized in Tab. 1 ($^{F}UO_2$, without notch), Tab. 2 ($^{F}UO_2$, with initial notch), Tab. 3 ($^{I}UO_2$, without notch) and Tab. 4 ($^{I}UO_2$, with initial notch). The dimensions of the specimen are depicted in Fig. 2.

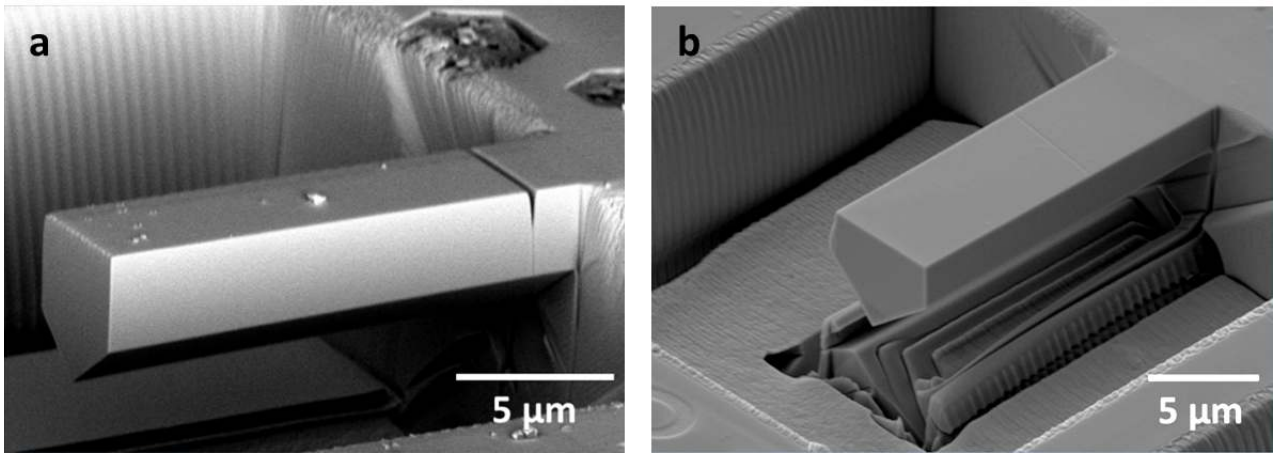

Figure 1: Micro-cantilever specimens a) with or b) without initial notch prepared in UO_2 fuel samples [9].

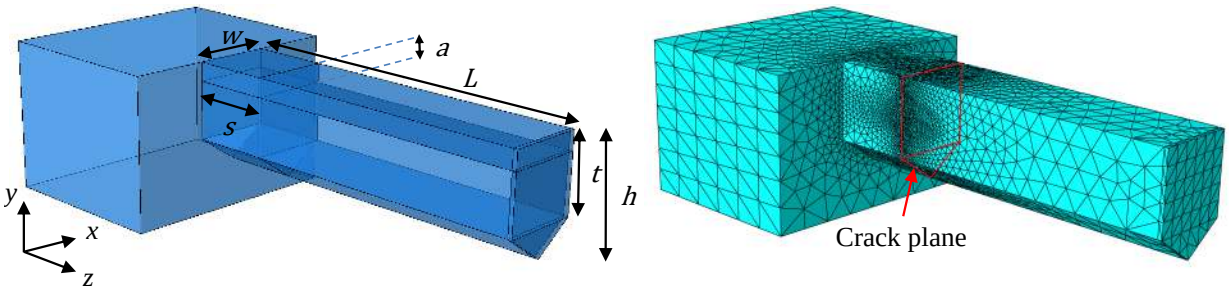

Figure 2: Specimen geometry and dimensions and typical FE mesh refined near the crack plane.

Tested plan	{100}	{100}	{110}	{110}	{111}	{111}
t (µm)	2.62	2.73	2.09	2.82	3.32	3.35
h (µm)	4.30	4.79	4.53	5.14	5.32	5.17
w (µm)	4.14	4.81	6.17	5.71	4.89	4.36
L (µm)	18.94	17.91	18.09	14.47	18.20	16.85
Failure force (mN) Experiments	1.88	2.09	2.62	2.47	2.36	2.29
Failure force (mN) Predictions	1.56	2.29	1.88	2.91	2.41	2.24

Table 1: Dimensions and failure force measured experimentally and obtained numerically for $^{\mathrm{F}}UO_2$ specimens with a controlled crystal orientation without initial notch.

Tested plan	{100}	{100}	{110}	{110}	{111}	{111}
t (µm)	2.91	3.03	3.19	2.53	2.40	2.84
h (µm)	4.76	5.21	5.76	3.94	5.13	4.86
w (µm)	4.51	5.06	5.74	3.40	6.04	4.82
L (µm)	14.43	13.41	10.77	12.29	14.21	15.22
s (µm)	2.70	2.39	2.47	3.66	3.19	3.34
a (µm)	1.32	1.28	1.45	1.25	1.32	1.12
Failure force (mN) Experiments	0.83	1.04	1.52	0.49	0.93	0.59
Failure force (mN) Predictions	0.75	1.12	1.58	0.38	1.00	0.59

Table 2: Dimensions and failure force measured experimentally and obtained numerically for $^{\mathrm{F}}UO_2$ specimens with a controlled crystal orientation with an initial notch.

Tested plan	{100}	{100}	{110}	{110}	{110}	{111}	{111}
t (µm)	2.72	3.35	3.19	3.91	2.66	3.96	2.55
h (µm)	4.66	5.92	5.73	5.98	5.04	6.04	5.46
w (µm)	4.01	6.31	5.77	4.80	5.97	4.62	6.66
L (µm)	15.65	17.61	18.68	21.96	17.79	14.57	18.58
Failure force (mN) Experiments	2.13	5.62	2.95	2.32	2.50	2.76	2.94
Failure force (mN) Predictions	2.51	5.45	2.92	2.42	2.43	3.12	2.5

Table 3: Dimensions and failure force measured experimentally and obtained numerically for $^{\mathrm{I}}UO_2$ specimens with a controlled crystal orientation without initial notch.

Tested plan	{100}	{100}	{100}	{110}	{110}	{111}	{111}	{111}	{111}
t (µm)	3.00	2.83	2.50	3.00	3.54	3.87	3.65	4.12	2.60
h (µm)	5.07	4.69	5.40	5.38	5.43	6.19	5.70	5.89	4.81
w (µm)	4.49	4.09	6.63	5.77	3.89	5.27	4.53	3.92	5.35
L (µm)	10.10	13.67	15.55	18.20	18.95	12.46	12.62	13.93	14.21
s (µm)	4.04	1.99	3.83	3.41	2.28	3.52	2.61	1.73	3.73
a (µm)	0.98	0.98	0.96	0.92	0.96	0.91	0.91	0.92	1.09
Failure force (mN) Experiments	1.20	0.63	1.25	1.13	0.71	1.49	1.04	0.88	0.80
Failure force (mN) Predictions	1.21	0.50	1.13	1.14	0.72	1.56	1.03	0.84	0.68

Table 4: Dimensions and failure force measured experimentally and obtained numerically for $^{\mathrm{I}}UO_2$ specimens with a controlled crystal orientation with an initial notch.

2.3. Testing procedure

Bending tests are performed using a nano-indenter with a cube corner tip inside the chamber of a Scanning Electron Microscope (SEM). A detailed description of the testing procedure is given in [9]. Specimens with or without initial notch exhibit a linear elastic behavior before brittle fracture. The measured forces at failure are given in Tabs. 1-4.

2.4. Fracture surfaces

SEM observations of the broken specimen fracture surfaces indicate three different possible fracture scenarii:

i) Fracture occurs from the initial notch for every notched samples (Fig. 3a).

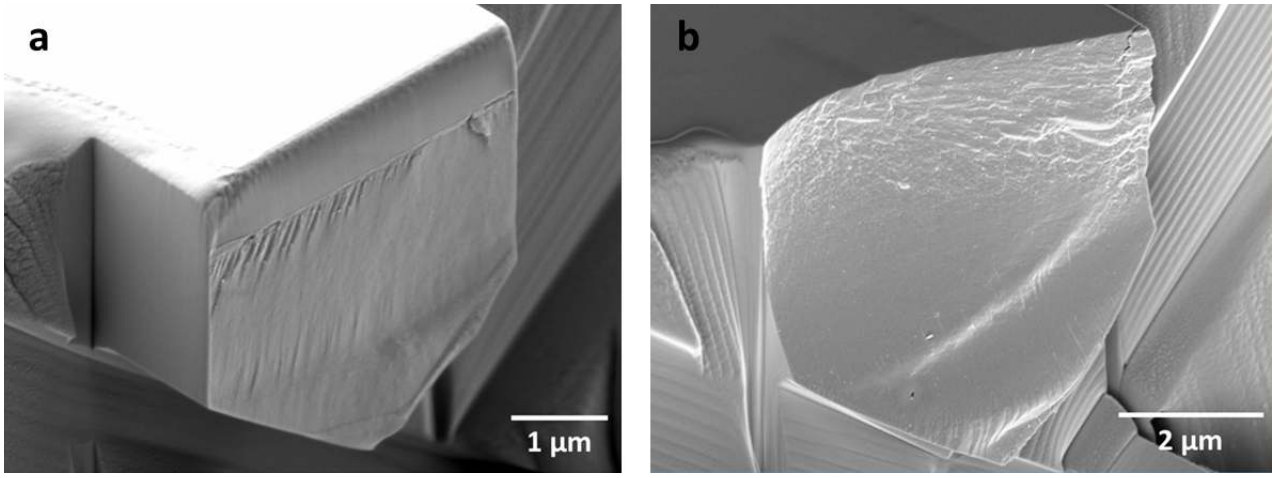

Figure 3: Fracture surface SEM images of $^{F}UO_2$ broken micro-cantilevers (a) with and (b) without initial notch

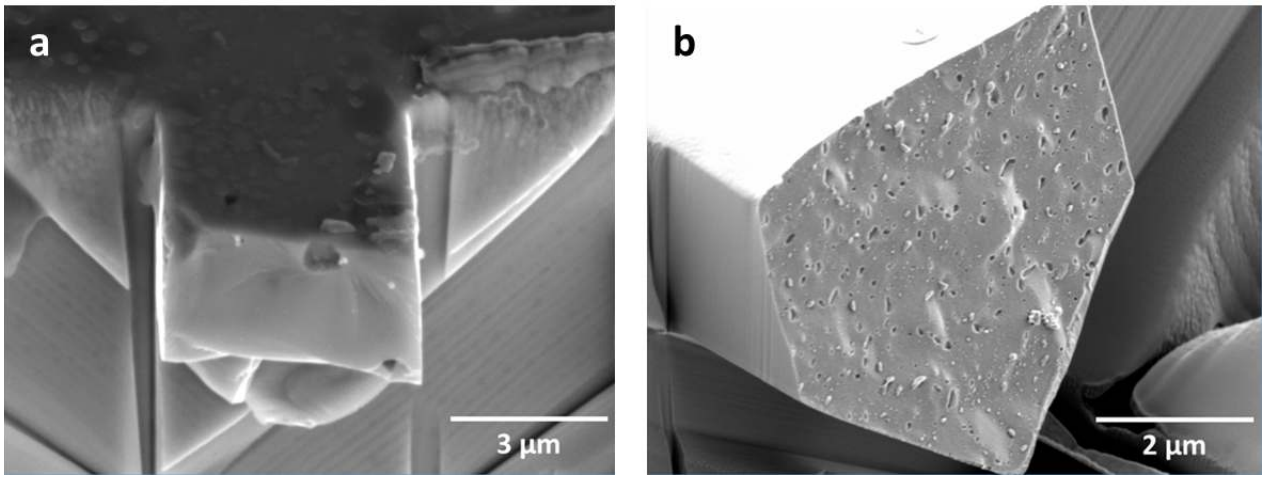

Figure 4: SEM images of (a) $^{F}UO_2$ and (b) $^{I}UO_2$ broken micro-cantilevers exhibiting (a) a single pore or (b) a network of porosities on the fracture surface.

ii) Fracture occurs from the specimen surface undergoing tension at its maximum location for samples without initial notch, *i.e.* near the cantilever basis (Fig. 3b). It can be noted that the fracture surface morphology depends on the tested crystal plane [9].

iii) Fracture occurs from a pore located near the surface undergoing tension in a sample without initial notch (Fig. 4a). The dimensions of the specimens for which a pore lies on the fracture surface are summarized in Tab. 5 for $^{F}UO_2$ specimens and in Tab. 6 for $^{I}UO_2$ specimens.

Tested plan	{100}	{111}	{111}	{111}
t (µm)	3.45	3.19	2.82	2.42
h (µm)	5.42	5.24	5.1	4.52
w (µm)	4.47	4.76	4.47	4.47
L (µm)	16.97	16.69	16.81	16.72
s (µm)	3.52	4.15	0.0	4.76
d (µm)	0.34	0.66	0.38	0.52
y (µm)	2.91	2.68	2.54	2.14
Failure force (mN) Experiments	2.64	2.31	1.54	1.40
Failure force (mN) Predictions	3.16	2.35	1.95	1.68

Table 5: Dimensions and failure force measured experimentally and obtained numerically for $^{\mathrm{F}}UO_2$ specimens without initial notch and showing a pore on the fracture surface (diameter d, pore center ordinate y, see Fig. 8).

Tested plan	{111}	{100}
t (µm)	2.75	2.61
h (µm)	4.46	5.50
w (µm)	5.08	6.54
L (µm)	18.14	17.42
s (µm)	9.48	5.05
d (µm)	2.66	0.90
y (µm)	1.66	2.12
Failure force (mN) Experiments	1.14	2.81
Failure force (mN) Predictions	1.28	2.61

Table 6: Dimensions and failure force measured experimentally and obtained numerically for $^{\mathrm{I}}UO_2$ specimens without initial notch and containing a pore on the fracture surface (diameter d, pore center ordinate y, see Fig. 8).

It can be observed that the fracture surfaces of $^{\mathrm{F}}UO_2$ specimens are relatively smooth (Fig. 3 and 4a). On the contrary, irradiation induces flaws such as small porosities or fission product precipitates (Fig. 4b), which are mainly located near grain boundaries [10].

3. Fracture modeling and simulation

This section is dedicated to the numerical models used for fracture prediction and the FE simulations of micro-cantilever specimens.

3.1. The coupled criterion

The coupled criterion proposed by Leguillon [16] allows the prediction of the initatiation loading level and crack surface. It states that a crack can nucleate only if two separate conditions are simultaneously met. The first one states that the opening stress σ_{nn} must be higher than the strength σ_c on the whole crack surface prior to crack initiation. The second condition compares the potential energy variation (ΔW) to crack surface (S) ratio to the material fracture toughness G_c. Under the assumption of linear elasticity and small deformations, since the stress is proportional to the applied displacement (denoted U_0) and the energy is proportional to the square applied displacement, these conditions write:

$$\sigma_{nn}(S) = \xi(S)U_0 \geqslant \sigma_c, \tag{1}$$

and:

$$G_{inc}(S) = -\frac{\Delta W}{S} = A(S)U_0^2 \geqslant G_c, \tag{2}$$

where G_{inc} is called the incremental energy release rate, ξ and A depend on the geometry and material behavior. The initiation loading is determined as the minimum loading for which both conditions are fulfilled. In case of monotonically decreasing stress and monotonically increasing incremental energy release rate, initiation crack surface S_c is obtained by combining Eqn. (1) and Eqn. (2):

$$\frac{A(S_c)}{\xi(S_c)^2} = \frac{G_c}{\sigma_c^2}. \tag{3}$$

The initiation loading is then determined using either Eqn. (1) or (2)

$$U_c = \frac{\sigma_c}{\xi(S_c)} = \sqrt{\frac{G_c}{A(S_c)}}. \tag{4}$$

Crack initiation surface S_c and loading level U_c are determined using Eqn. (3) and (4), which involve the functions A and ξ. The computation of ξ requires only one calculation on

the structure without crack, whereas several calculations with increasing crack surfaces are necessary to determine A. This is done by successively releasing the nodes lying on the crack surface in order to compute the potential energy for different crack surfaces.

Solving Eqn. (3) requires the knowledge of the material strength and fracture toughness. A major advantage of the coupled criterion is the implementation of these parameters only during the post-processing of the FE calculations. Indeed, the function ξ and A can be obtained without any assumptions on G_c and σ_c. Once these two functions are determined, the CC solution can be obtained for several parameter couples without any extra FE calculations. It only requires solving again Eq. (3). Therefore, this approach is particularly well suited to be used for the identification of the strength and fracture toughness (*cf.* Section 4) if the crack path is a priori known. Otherwise, the approach may become computationally more costly, especially if the crack is described by several parameters [28, 39] .

3.2. Cohesive zone modeling

Another approach for fracture prediction is cohesive zone modeling, first introduced in [18, 19]. This approach basically consists in defining a relation between the opening displacement δ and the cohesive traction T acting between two surfaces. Debonding between the two surfaces occurs only if the traction reaches the strength σ_c. When the traction has reached this critical value, the opening displacement increases with a decrease in the cohesive traction until it attains a critical opening displacement δ_c for which the traction is zero, which corresponds to the local nucleation of a crack. The area under the traction-opening displacement profile corresponds to the material fracture toughness G_c. Therefore, similarly to the CC, fracture is also based on both stress and energy requirements since damage does not occur provided that the traction is smaller than the strength, and a sufficient amount of energy must be dissipated to trigger failure.

In addition to the strength and fracture toughness, required as inputs, a third parameter intervines in CZM: The traction-opening displacement profile. This parameter mainly has an influence on dynamic phenomena such as crack initiation [28, 44, 45], crack branching or unstable propagation [28, 46], whereas similar results are obtained whatever the chosen profile in case of stable rectilinear crack propagation [45, 46] provided the characteristic length is small with respect to the specimen dimensions.

It was shown that the profile can be identified by confrontation to experimental data [47] or numerical results obtained with the CC [28]. In the following, we consider a bilinear traction-opening displacement profile, which reads

$$T = \begin{cases} K\delta & \text{if } \delta \leq \frac{\sigma_c}{K}, \\ (\frac{\delta_c - \delta}{\delta_c - \frac{\sigma_c}{K}})\sigma_c & \text{if } \frac{\sigma_c}{K} \leq \delta \leq \delta_c, \\ 0 & \text{if } \delta \geq \delta_c. \end{cases} \tag{5}$$

The parameter K is an artificial stiffness that must be high enough so that it ensures the continuity of the displacement field if the traction is smaller than σ_c, *i.e.* it must not affect the overall rigidity of the model. However, the larger K the smaller the time increments required to solve the problem due to a poorer convergence. Therefore, K has to be carefully chosen so that (i) results are not artificially spoilt and (ii) calculation time is not redhibitory because of too small time increments. In practice, several values are tested and we choose the smallest value for which the results (for instance the failure force) are not influenced.

A major advantage of CZM compared to the CC is that there is no need to assume a crack front profile provided the knowledge of the crack path. Possible crack fronts can be determined based on the stress isocontours when employing the CC [37, 38, 48, 49], but this approach may not be straightforward to implement in presence of a large amount of porosities. CZM are more suitable in this case since the crack plane is a priori known. This approach is used in Section 5 to assess the influence of either a big pore or a network of small porosities on the specimen fracture.

3.3. Finite element model of micro-cantilever specimens

3.3.1. Micro-cantilever specimens

A FE model of micro-cantilever is set up using Abaqus^{TM}/Standard. The dimensions of the specimen containing an initial notch are depicted in Fig. 2. The same geometry is used for specimens without notch (a=0). Dirichlet boundary conditions are imposed in order to simulate the indenter induced beam bending. A local displacement in (Oy) direction is imposed at the location of the contact between the indenter and the specimen. An area where the beam is clamped is also modeled, with a null imposed normal displacement on its

external faces.

UO_2 single crystal exhibits a cubic symmetry in the main crystal directions with the following elastic constants : C_{11}=396 GPa, C_{12}=121 GPa and C_{44} =64.1 GPa. The local orientation of the crystal is defined so that the normal to the tested fracture plane ({100}, {110} or {111} crystal orientation) corresponds to the beam neutral axis direction (Oz).

The mesh consisting of 10-nodes tetrahedrons is refined near the fracture plane. Whether using CZM or CC, a sufficiently fine mesh must be adopted in order to correctly describe fracture, *i.e.*, to account for a fine description of the process zone when using CZM and to capture the initiation surface when employing the CC. Both quantities depends on the material properties and the specimen geometry, and it can be shown that they are related to the material characteristic length $L_{mat} = \frac{EG_c}{\sigma_c^2}$ [34, 50], where E is the Young's modulus in the beam neutral axis direction. In practice, the mesh size must be a fraction of this characteristic length and we choose a mesh size to characteristic length ratio at most 1/50. In the present case of inverse identification approach, for which the parameters are not known *a priori*, the minimum mesh size is chosen as 1/50 of the minimum characteristic length obtained among all the tested (G_c, σ_c) couples.

3.3.2. Porosity modeling

The FE model presented in the previous section offers a good representation of the smooth fracture surfaces observed for specimens without flaws (*cf.* Fig. 3). Experimental observations highlight the possible presence of either a single pore (*cf.* Fig. 4a) or a network of small porosities (*cf.* Fig. 4b), which may influence the specimen fracture.

We account for these porosities in the FE model by explicitly integrating them in the specimen geometry. We distinguish two possible cases observed experimentally, namely a pore (Fig. 5a) or a diffuse network of porosities lying on the crack plane (Fig. 5b). In both cases we assume that the porosities exhibit an idealized spherical shape. Boolean operations between the initial geometry and the spheres are performed in order to obtain the geometry including the porosities. Moreover, the same sphere radius is assumed for all the network porosities. The porosity network is obtained by a random sampling of the porosity centers on the crack plane so that the porosity surface fraction satisfies a prescribed value. The minimum mesh

size around the porosities is at most one tenth of the porosity diameter. Zero thickness 6-nodes cohesive zone elements are inserted on the crack surface including either the pore or the porosity network, which is achieved by doubling the nodes lying on the crack surface.

4. Parameter identification

4.1. Identification approach

The CC allows the prediction of the failure force providing the knowledge of the material strength and fracture toughness. In the present case, these parameters are not known therefore the aim is to determine them by indirect confrontation of the predicted failure forces to experimental measured one. The identification approach consists in determining the parameter couple (G_c, σ_c) that minimizes a residuals R quantifying the difference between N predicted and measured failure forces:

$$R^2(G_c, \sigma_c) = \sum_{i=1}^{N} (F_i^n(G_c, \sigma_c) - F_i^e)^2, \tag{6}$$

where $F_i^n(G_c,\sigma_c)$ is the failure force predicted numerically with the coupled criterion using the strength σ_c and fracture toughness G_c for the specimen #i, and F_i^e is the experimentally measured failure for the same specimen. We remind that some of the tested specimens contain an initial notch, therefore their contribution to the residuals is likely to be more influenced by fracture toughness than strength variation, whereas a strength variation is more likely to influence the failure force corresponding to specimens without notch. The minimization problem is solved by determining the couple (G_c^*, σ_c^*) minimizing the residuals R. A gradient descend approach is employed in order to determine the residuals minimum. It requires

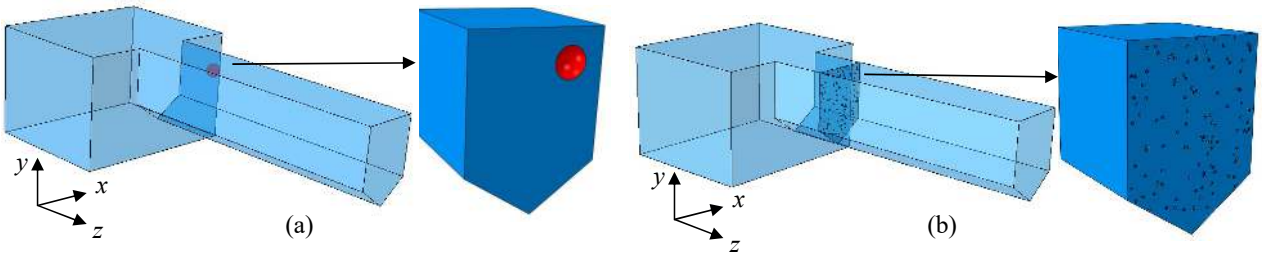

Figure 5: Geometry of a specimen containing (a) a pore or (b) a network of small porosities.

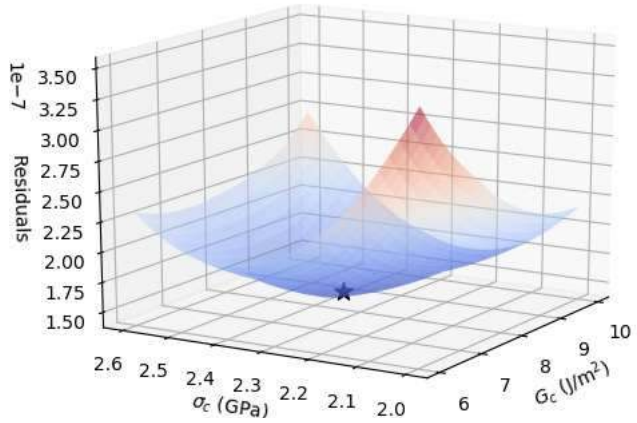

Figure 6: Residuals as a function of G_c and σ_c, the residuals minimum is indicated by a star.

the failure force calculation corresponding to several couples (G_c, σ_c). This calculation only requires solving Eqn. (3) for these parameters, which makes the minimization procedure computationally very efficient. The possibility to vary (G_c, σ_c) only in the FE calculation post-processing step is a major advantage of the CC compared to CZM. Indeed, the latter would require as many FE calculations as tested (G_c, σ_c) couples in the minimization procedure. An example of residuals variation as a function of strength and fracture toughness if depicted in Fig. 6. It can be seen that the residuals exhibit a well-established minimum so that the gradient descend approach is not likely to not fall into another possible local minimum.

4.2. Results

The results of the identification approach are gathered in Tab. 7. The identification is established based on failure forces corresponding to specimens without porosities. The failure forces obtained numerically with the identified parameters for these specimens are summarized in Tabs. 1-4. The uncertainty intervals given in Tab. 7 are estimated by applying the identification procedure while successively removing one of the tests in the residuals calculation. It allows determining other couples of parameters among which the minimum/maximum values of G_c and σ_c define the uncertainty interval. It can be noted that the identified strength is much larger than the strength measured on UO_2 macroscopic specimens, *i.e.* around 100-200 MPa [5, 6, 8, 51, 52]. The fracture toughness is in the same order of magnitude as the

one measured on macroscopic specimens [6]. It leads to characteristic lengths around 100 μm for macroscopic specimens and around 1 μm for micron-scale specimens. This size effect can be explained by the fact that the properties determined using the micron scale specimens are representative of the grain properties, whereas a macroscopic specimen contain grains, grain boundaries and possible intrinsic flaws that define its microstructure. The strength of macroscopic specimens thus depends on microstructure features such as the grain size or the presence of intrinsic flaws [34, 53] and therefore appears to be smaller than that of a single grain specimen.

The identified parameters allows discussing about the influence of irradiation on UO_2 failure. First, it can be observed that the strength does not seem to be influenced by irradiation. Indeed, the variation between the identified strength for $^{F}UO_2$ and $^{I}UO_2$ lies within the measurement uncertainty interval whatever the crystal orientation. On the contrary, it seems that irradiation induces a decrease in fracture toughness. This is clearly observed for {100} and {111} orientation, for which the fracture toughness respectively decreases from around 10 J/m^2 and around 8 J/m^2 to around 5 J/m^2. It can be noted that this trend is not observed for {110} specimens, for which no significant influence of the irradiation is highlighted either on fracture tougness or on strength. It may be due to the fact that for some of {110} specimens without initial notch, fracture did not occur on the selected crystal plane, as shown in [10].

Sample - fracture plane	G_c (J/m^2)		σ_c (GPa)	
$^{F}UO_2$ - {100}	10.4	[8.6 11.7]	2.49	[2.21 3.15]
$^{I}UO_2$ - {100}	4.98	[4.35 5.26]	3.24	[2.70 3.34]
$^{F}UO_2$ - {110}	9.86	[9.11 12.6]	1.77	[1.41 2.77]
$^{I}UO_2$ - {110}	11.4	[11.27 12.79]	1.80	[1.75 1.85]
$^{F}UO_2$ - {111}	7.80	[7.74 7.91]	1.87	[1.83 1.92]
$^{I}UO_2$ - {111}	4.79	[4.61 5.65]	1.57	[1.36 1.90]

Table 7: Fresh and irradiatied UO_2 fracture toughness and strength optima and uncertainty intervals identified by minimization of the residuals for the different crystal orientations.

5. Influence of porosities on specimen fracture

This section is dedicated to porosities and their influence on UO_2 specimen failure.

5.1. Single pore

We first study the influence of a pore that is likely to initiate the specimen fracture as observed experimentally on some specimens (*cf.*, for instance, Fig. 4a). Fig. 7 shows the stress distribution along the crack surface prior to fracture in presence of a pore located either near the specimen surface undergoing tension (Fig. 7a-c) or at around half the specimen thickness from this surface (7d-f). It can be observed that far from the pore, the stress distribution

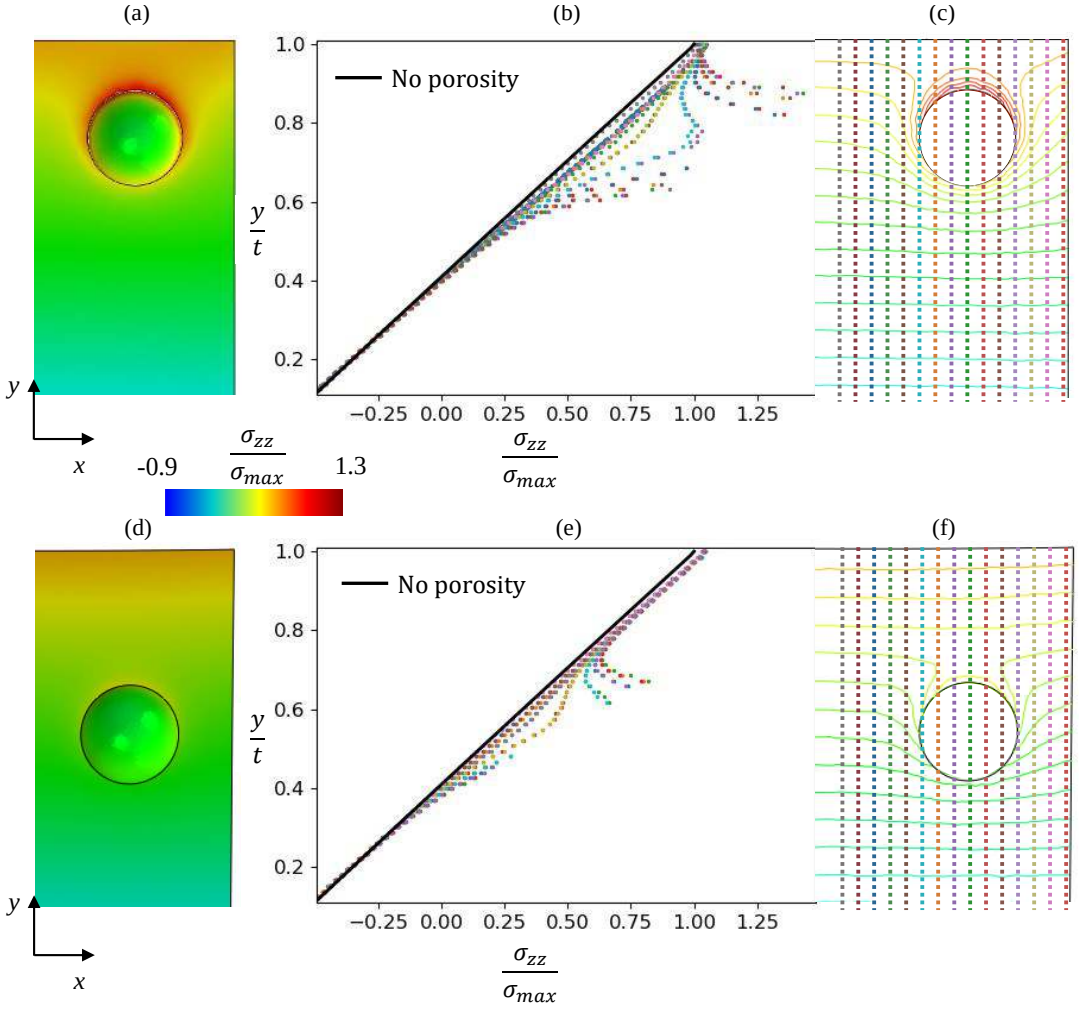

Figure 7: (a,d) Opening stress field and (b,e) stress variation (normalized by the maximum stress reached without pore σ_{max}) along lines depicted in (c,f) on the crack surface containing a pore located either (d-f) in the specimen center or (a-c) near the surface undergoing tension prior to fracture.

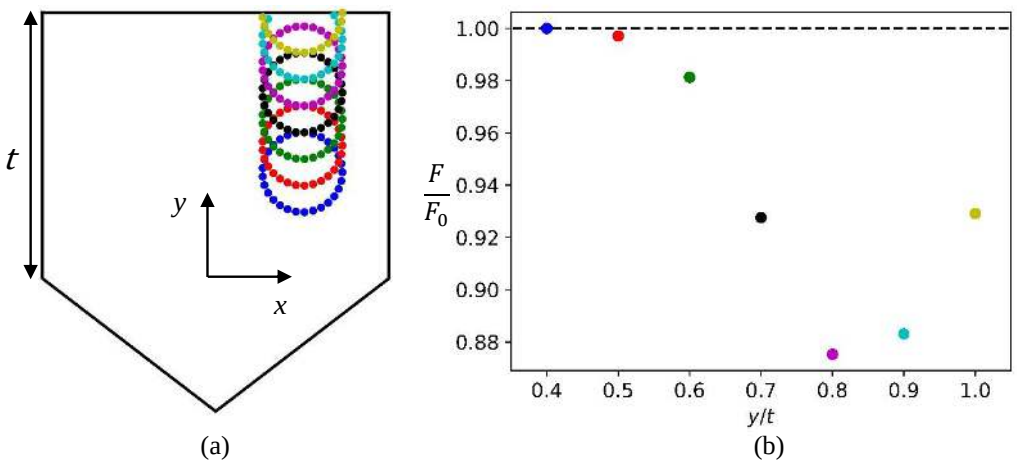

Figure 8: Failure force (normalized by the failure force without pore F_0) as a function of the pore position y to thickness t ratio for a fixed pore diameter.

is similar to that without pore. However, not surprisingly, there is stress concentration near the pore which leads to two different configurations depending on the pore position in the specimen thickness.

- If the pore is located far enough from the specimen surface undergoing tension, the local stress increase remains smaller than the stress maximum that is reached at the specimen surface. In this case, one may expect that the crack initiates from the specimen surface rather than from the pore, which may not influence the specimen fracture.

- If the pore is located close enough from the specimen surface undergoing tension, the local stress increase due to the pore overcomes the maximum stress reached at the specimen surface. In this case, the pore may be a privileged location for crack initiation and it is more likely to trigger premature fracture of the specimen.

Fig. 8 displays the failure force as a function of the pore location in the specimen thickness for a fixed pore size. It can be observed that the failure force increases when the pore center location passes from 0.8 (near the top surface) to 0.4 (near the center) specimen thickness and tends towards the failure force obtained for a specimen without pore, which is consistent with the conclusion drawn based on the stress distribution analysis. It can also be observed that if the failure force increase when the porosity center location passes from 0.8 to 1 specimen thickness. However, not only the position of the pore but also the size changes since for pore

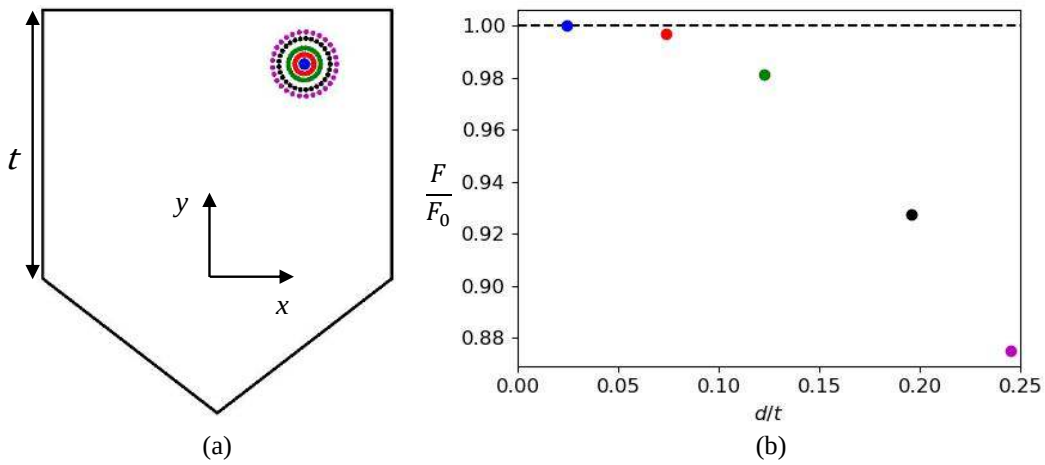

Figure 9: Failure force (normalized by the failure force without pore F_0) as a function of the pore diameter d to thickness t ratio for a fixed pore center location.

center located at more than 0.8 thickness, the pore size also changes, the pore diameter being approximately equal to 0.3 thickness.

Fig. 9 displays the failure force as a function of the pore diameter for a fixed pore center location. Not surprisingly, the failure force decreases for decreasing pore size and tends towards the failure force obtained for a specimen without pore.

The failure of specimens containing a pore on the fracture surface (*cf.* Tabs 5 and 6) is assessed using the strength and fracture toughness optima (*cf.* Tab 7) determined in Section 4. A blind prediction of the failure force is established accounting for the force decrease due to the pore. The predicted failure forces accounting for these porosities, summarized in Tab. 5, are in satisfying agreement with the ones measured experimentally.

5.2. Network of small porosities

A network of small porosities may be observed on the fracture surface, *cf.* for instance Fig. 4b. The parameter identification proposed in Section 4 allows determining the influence of irradiation on UO_2 strength and fracture toughness, but the possible presence of porosities on the crack surface was not taken into account in the identification.

Fig. 10 shows the stress distribution on the crack plane prior to fracture in presence of a porosity network. It can be seen that the overall stress variation is locally affected by porosities that act as stress concentrators. The porosities are likely to trigger local stress increase so that it overcomes the stress maximum attained at the specimen surface undergoing tension. Therefore, it is expected that the porosity network may induce a decrease in the failure force. Figs. 11 and 12 depicts the failure force variation as a function of either the porosity diameter (Fig. 11) or the porosity surface fraction (Fig. 12). It can be noted that all the porosities in the network have the same radius.

Since the porosity network is obtained using a random sampling of the porosity center location, the failure force has been computed for three porosity networks for each configuration. Thus, the failure force variation as a function of either the porosity diameter or the surface fraction is displayed as error bars corresponding to the three failure forces obtained. A clear influence of the porosity surface fraction for fixed porosity diameter is highlighted since the failure force increases with decreasing porosity surface fraction and tends towards

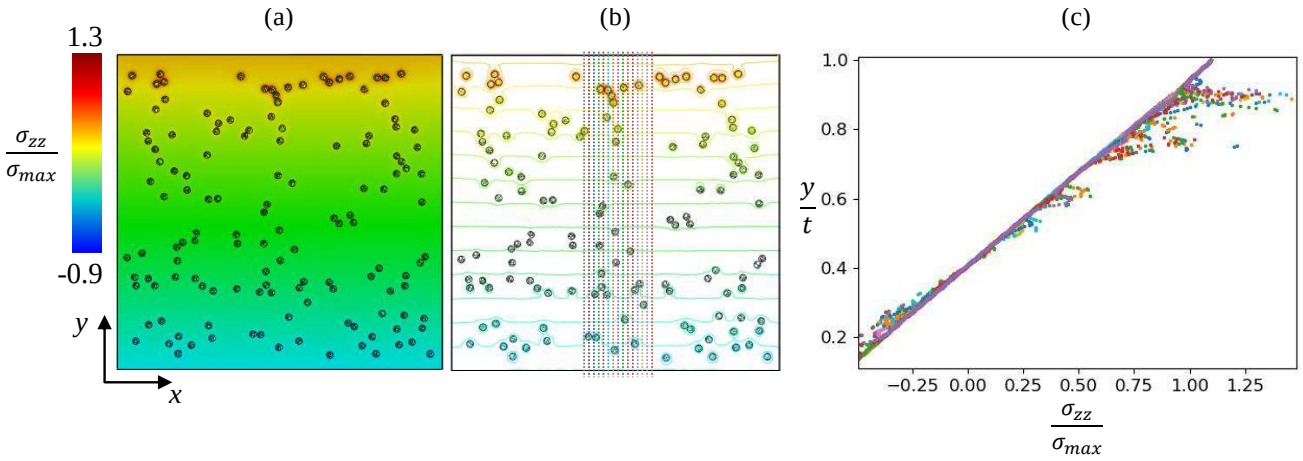

Figure 10: (a) Opening stress field and (c) stress variation along lines depicted in (b) on the crack surface containing a network of small porosities.

the failure force of a specimen without porosity. On the contrary, the porosity diameter for a fixed surface fraction barely influences the failure force.

The porosity surface fraction quantified experimentally on irradiated specimens is around 7%, which may lead to force decrease up to around 8% compared to the case without porosity. The same order of magnitude variation may thus be expected in the strength and toughness if the porosity network was taken into account for the parameter identification.

6. Conclusion

We determined the strength and toughness of either fresh or irradiated UO_2 along three crystal orientations by means of inverse identification on micro-cantilever tests. The identification resulted from failure force prediction of micron scale specimens with or without initial notch obtained numerically using the coupled criterion.

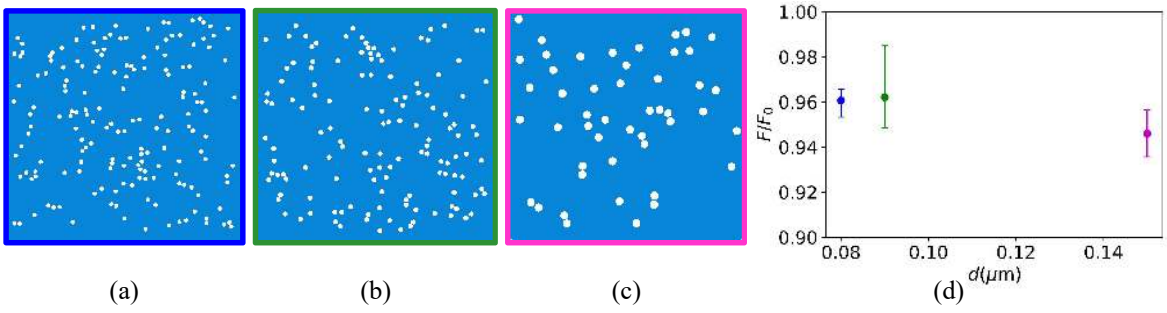

Figure 11: Porosity network distribution on the crack surface for (a) 80, (b) 90 and (c) 150nm porosity diameter with 5% surface fraction. Failure force variation as a function of the porosity diameter obtained for three different porosity network distributions with the same characteristics.

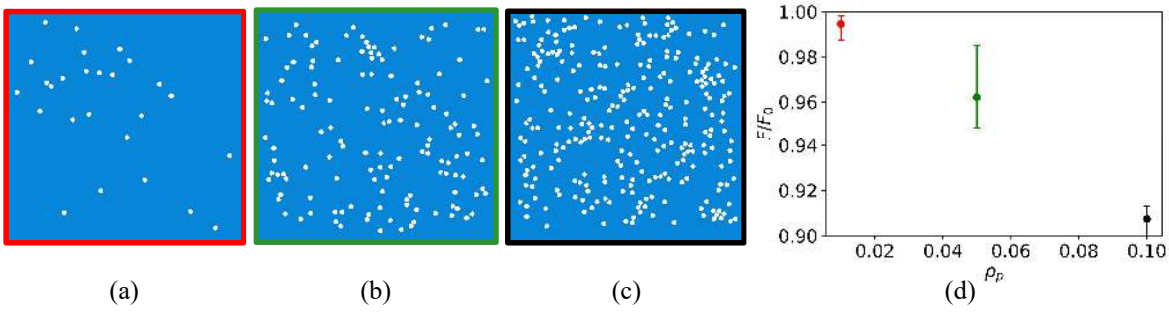

Figure 12: Porosity network distribution on the crack surface for (a) 1%, (b) 5% and (c) 10% porosity surface fraction with 90nm porosity diameter. Failure force variation as a function of the porosity surface fraction obtained for three different porosity network distributions with the same characteristics.

The influence of irradiation is notable since the fracture toughness decreases respectively from around 10 J/m^2 or 8 J/m^2 to around 5 J/m^2 for {100} and {111} orientations. On the contrary, the strength does not seem to be affected by irradiation since the identified values remains in the same order of magnitude as the measurement uncertainty.

The presence of a pore leads to a decrease in the failure force only if the pore is close enough to the specimen surface sollicitated under tension. The closer to the specimen surface or the larger the pore, the larger the force decrease.

Premature fracture may also occur due to a network of small porosities, which are observed experimentally on fracture surfaces of irradiated specimens. The porosity network induces a force decrease compared to the case without porosities. Moreover, this force decrease mainly depends on the porosity surface fraction but barely depends on their size for a fixed surface fraction.

Acknowledgements

This research project was mainly funded by INSA-Lyon and CEA, and was also financially supported by EDF and Framatome.

References

[1] C. Nonon, S. Lansiart, C. Struzik, D. Plancq, S. Martin, G. Decroix, O. Rabouille, S. Beguin, B. Julien, Impact of fuel microstructure on pci behaviour, Proc. a Tech. Comm. Meet. IAEA (2004).

[2] D. Lespiaux, J. Noirot, P. Menut, Post-test examinations of high burnup PWR fuels submitted to RIA transients in the CABRI facility, Proc. Int. Top. Meet. LWR fuel Perform. (1997).

[3] NEA, Report on fuel fragmentation relocation and dispersal, Tech. rep., Nuclear Energy Agency (2016).

[4] B. Michel, J. Sercombe, G. Thouvenin, A new phenomenological criterion for pellet-cladding interaction rupture, Nucl. Eng. Des. 238 (7) (2008) 1612–1628.

[5] B. Michel, J. Sercombe, G. Thouvenin, R. Chatelet, 3d fuel cracking modelling in pellet cladding mechanical interaction, Eng. Fract. Mech. 75 (11) (2008) 3581–3598.

[6] A. G. Evans, R. W. Davidge, The strenght and fracture of stoichoimetric polycristalline uo2, J. Nucl. Mater. 33 (33) (1969) 249–260.

[7] R. F. Canon, J. T. A. Roberts, R. J. Beals, Deformation of uo2 at high temperatures, J. Am. Ceram. Soc. 54 (2) (1971) 105–112.

[8] J. Gatt, J. Sercombe, I. Aubrun, J. Ménard, Experimental and numerical study of fracture mechanisms in uo2 nuclear fuel, Eng. Fail. Anal. 47 (2015) 299–311.

[9] R. Henry, I. Zacharie-Aubrun, T. Blay, S. Chalal, J. Gatt, C. Langlois, S. Meille, Fracture properties of an irradiated pwr uo2 fuel evaluated by micro-cantilever bending tests, J. Nucl. Mater. (2020). doi:10.1016/j.jnucmat.2020.152209.

[10] R. Henry, I. Zacharie-Aubrun, T. Blay, N. Tarisien, S. Chalal, X. Iltis, J. Gatt, C. Langlois, , S. Meille, Irradiation effects on the fracture properties of uo2 fuels studied by micro-mechanical testing, J. Nucl. Mater. (2020). doi:10.1016/j.jnucmat.2020.152179.

[11] D. Di Maio, S. Roberts, Measuring fracture toughness of coatings using focused-ion-beam-machined microbeams, J. Mater. Res. 20 (02) (2005) 299–302.

[12] D. Frazer, B. Shaffer, K. Roney, H. Lim, B. Gong, P. Peralta, P. Hosemann, Small-scale mechanical testing of uo2, Trans. Amer. Nucl. Soc. 116 (2017) 485–487.

[13] S. Johansson, J. a. . Schweitz, L. Tenerz, J. Tirén, Fracture testing of silicon microelements in situ in a scanning electron microscope, J. Appl. Phys. 63 (10) (1988) 4799–4803.

[14] E. Camposilvan, O. Torrents, M. Anglada, Small-scale mechanical behavior of zirconia, Acta Mater. 80 (2014) 239–249.

[15] K. Matoy, T. Detzel, M. Muller, C. Motz, G. Dehm, Interface fracture properties of thin films studied by using the micro-cantilever deflection technique, Surf. Coatings Technol. 204 (6-7) (2009) 878–881.

[16] D. Leguillon, Strength or toughness? a criterion for crack onset at a notch, Eur. J. Mech. - A/Solids 21(1) (2002) 61–72.

[17] A. Doitrand, R. Henry, J. Chevalier, S. Meille, Revisiting the strength of micron-scale ceramic platelets., J. Am. Ceram. Soc. 00 (2020) 1–10.

[18] G. I. Barenblatt, The formation of equilibrium cracks during brittle fracture. general ideas and hypotheses. axially-symmetric cracks, J. App. Math. Mech. 23 (3) (1959) 622–636.

[19] D. S. Dugdale, Yielding of steel sheets containing slits, J. Mech. and Phy. Sol. 8 (2) (1960) 100–104.

[20] P. Weißgraeber, D. Leguillon, W. Becker, A review of finite fracture mechanics: crack initiation at singular and non-singular stress raisers, Archive Appl. Mech. 86(1-2) (2016) 375–401.

[21] N. Moës, J. Dolbow, T. Belytschko, A finite element method for crack growth without remeshing, Int. J. Num. Meth. Engng. 46 (1) (1999) 131–150.

[22] N. Moës, C. Stolz, P.-E. Bernard, N. Chevaugeon, A level set based model for damage growth: The thick level set approach, Int. J. Num. Meth. Engng. 86 (3) (2011) 358–380.

[23] B. Bourdin, G. A. Francfort, J.-J. Marigo, The Variational Approach to Fracture, Springer Netherlands, 2008.

[24] C. Miehe, F. Welschinger, M. Hofacker, Thermodynamically consistent phase-field models of fracture: Variational principles and multi-field FE implementations, Int. J. Num. Meth. Engng. 83 (10) (2010) 1273–1311.

[25] G. Molnár, A. Gravouil, 2d and 3d abaqus implementation of a robust staggered phase-field solution for modeling brittle fracture, Fin. Elem. Anal. Des. 130 (2017) 27 – 38.

[26] P. Cornetti, M. M. noz Reja, A. Saporaand, A. Carpinteri, Finite fracture mechanics and cohesive crack model: weight functions vs. cohesive laws, Int. J. Sol. Struct 156-157 (2019) 126–136.

[27] P. Cornetti, A. Sapora, A. Carpinteri, Short cracks and V-notches: Finite fracture mechanics vs. cohesive crack model, Engng. Fract. Mech. 168 (2016) 2–12.

[28] A. Doitrand, R. Estevez, D. Leguillon, Comparison between cohesive zone and coupled criterion modeling of crack initiation in rhombus hole specimens under quasi-static compression, Theor. App. Fract. Mech 99 (2019) 51–59.

[29] I. G. García, M. Paggi, V. Mantič, Fiber-size effects on the onset of fiber–matrix debonding under transverse tension: A comparison between cohesive zone and finite fracture mechanics models, Engng. Fract. Mech. 115 (2014) 96–110.

[30] C. Henninger, D. Leguillon, E. Martin, Crack initiation at a v-notch-comparison between a brittle fracture criterion and the dugdale cohesive model, C. R. Mecanique 335 (2007) 388–393.

[31] E. Martin, T. Vandellos, D. Leguillon, N. Carrère, Initiation of edge debonding: coupled criterion versus cohesive zone model, Int. J.Fract 199 (2016) 157–168.

[32] B. Poitou, E. Martin, N. Carrère, D. Leguillon, J. M. Gatt, Amorçage de fissure au voisinage des interfaces fibre/matrice : comparaison d'un critère mixte et des modèles de zone cohésive, 18$^{\text{eme}}$ Congrès Français de Mécanique (2007).

[33] E. Martin, D. Leguillon, N. Carrère, A coupled strength and toughness criterion for the prediction of the open hole tensile strength of a composite plate, Int. J. Sol. Struct. 49(26) (2012) 3915–3922.

[34] E. Martin, D. Leguillon, O. Seveček, R. Bermejo, Understanding the tensile strength of ceramics in the presence of small critical flaws, Engng. Fract. Mech. 201 (2018) 167–175.

[35] L. Ricardo, D. Leguillon, G. Parry, A. Doitrand, Modeling the thermal shock induced cracking in ceramics, J. Eur. Cer. Soc. 40 (2020) 1513–1521.

[36] D. Leguillon, An attempt to extend the 2d coupled criterion for crack nucleation in brittle materials to the 3d case, Theor. Appl. Fract. Mech. 74 (2014) 7–17.

[37] A. Doitrand, D. Leguillon, 3D application of the coupled criterion to crack initiation prediction in epoxy/aluminum specimens under four point bending, Int. J. Sol. Struct 143 (2018) 175–182.

[38] A. Doitrand, R. Estevez, D. Leguillon, Experimental characterization and numerical modeling of crack initiation in rhombus hole pmma specimens under compression, Eur. J. Mech. Sol. 76 (2019) 290–299.

[39] A. Doitrand, C. Fagiano, N. Carrère, V. Chiaruttini, M. Hirsekorn., Damage onset modeling in woven composites based on a coupled stress and energy criterion, Engng. Fract. Mech. 169 (2017) 189–200.

[40] T. Cardianels, K. Govers, B. Vos, S. Van Den Berghe, M. Verwerft, L. De Tollenaere, G. Maier, C. Delafoy, Chromia doped uo2 fuel: Investigation of the lattice parameter., J. Nucl. Mater. 424 (1-3) (2012) 252–260.

[41] A. Norton, S. Falco, N. Young, J. Severs, R. Todd, Microcantilever investigation of fracture toughness and subcritical crack growth on the scale of the microstructure in al2o3, J. Eur. Ceram. Soc. 35 (16) (2015) 4521–4533.

[42] B. Jaya, C. Kirchlechner, G. Dehm, Can microscale fracture tests provide reliable fracture toughness values ? a case study in silicon., J. Mater. Res. 30 (5) (2015) 686–698.

[43] R. Henry, T. Blay, T. Douillard, A. Descamps-Mandine, I. Zacharie-Aubrun, J. Gatt, C. Langlois, S. Meille, Local fracture toughness measurements in polycrystalline cubic zirconia using micro-cantilever bending tests, Mech. Mater. 136 (2019) 103086.

[44] G. Alfano, On the influence of the shape of the interface law on the application of cohesive-zone models., Compos. Sci. Tech. 66 (2006) 723–730.

[45] A. Doitrand, R. Estevez, M. Thibault, P. Leplay, Fracture and cohesive parameter identification of refractories by digital image correlation up to 1200°c, Exp. Mech. (2020). doi:10.1007/s11340-020-00584-7.

[46] V. Acary, Y. Monerie, Nonsmooth fracture dynamics using a cohesive zone approach, Tech. rep., Research Report RR-6032, INRIA (2006).

[47] J. Réthoré, R. Estevez, Identification of a cohesive zone model from digital images at the micron-scale, J. Mech. Phy. of Sol. 61 (6) (2013) 1407–1420.

[48] A. Doitrand, D. Leguillon, Comparison between 2D and 3D applications of the coupled criterion to crack initiation prediction in scarf adhesive joints, Int. J. Adh. Adh. 85 (2018) 69–76.

[49] A. Doitrand, D. Leguillon, Numerical modeling of the nucleation of facets ahead of a primary crack under modeI+III, Int. J. Fract. 123(1) (2018) 37–50.

[50] A. Turon, C. Dávila, P. Camanho, J. Costa, An engineering solution for mesh size effects in the simulation of delamination using cohesive zone models, Eng. Fract. Mech. 74 (2007) 1665–1682.

[51] K. Radford, Effect of fabrication parameters and microstructure on the mechanical strenght of uo2 fuel pellets., J. Nucl. Mater. 84 (1979) 222–236.

[52] M. Oguma, Effect of fabrication parameters and microstructure on the mechanical strenght of uo2 fuel pellets., J. Nucl. Mater. 19 (12) (1982) 1005–1014.

[53] D. Leguillon, E. Martin, O. Seveček, R. Bermejo, What is the tensile strength of a ceramic to be used in numerical models for predicting crack initiation?, Int. J. Fract. 212(1) (2018) 89–103.